

Detective Quantum Efficiency of the Timepix4 Hybrid Pixel Detector and its Application to Parallel-Beam Diffraction

Zhiyuan Ding ^{1,2}, Nina Dimova ³, Jonathan S. Barnard ²,
Giulio Crevatin ⁴, Liam O’Ryan ⁴, Richard Plackett ³,
Daniela Bortoletto ³, Angus I. Kirkland ^{1,2} and Marcus Gallagher-Jones ²

¹ Department of Materials, University of Oxford, Oxford, UK

² The Rosalind Franklin Institute, Harwell Campus, Didcot, UK

³ Department of Physics, University of Oxford, Oxford, UK

⁴ Quantum Detectors Ltd., Harwell Campus, Didcot, UK

Abstract

The detective quantum efficiency (DQE) and normalised noise power spectrum (NNPS) of the Timepix4 hybrid pixel detector in event-driven mode in TEM have been measured at 100 kV and 200 kV. In a raw data readout mode, the zero-frequency DQE exceeds 0.9 at both 100 kV and 200 kV. At the Nyquist frequency, the DQE remains above 0.2 at 100 kV but drops close to zero at 200 kV. Initial parallel-beam diffraction data from a polycrystalline gold nanoparticle sample is reported which shows that at 200 kV Timepix4 can detect weak diffracted information beyond a 75 mrad half-angle.

1 Introduction

The Timepix4 is the newest member of the Medipix family of readout ASICs [1]. As an event-based hybrid pixel detector with 195 ps event binning [2, 3], it has been widely used for the detection of high energy particles [4], X-rays [5–7] and photons from the visible to gamma rays [8–10]. In applications for transmission electron microscopy (TEM), the Timepix4 detector offers clear advantages for high timing resolution data recording. This is particularly important for data collection in various imaging geometries, including 4DSTEM [11–13], tomography [14, 15] and microED/3DED [16, 17], at low fluences which minimise radiation damage to the sample.

For practical applications in TEM, the detector response as a function of the electron beam energy and fluence requires characterisation. Quantitative measurements including the modulation transfer function (MTF) and detective quantum efficiency (DQE) are representative metrics that characterise the detector’s response to electron hits [18–20]. The MTF reflects the detector’s ability to resolve information as a function of spatial frequency [19]. The DQE reflects the transfer of information above noise across different spatial frequencies [21, 22].

Using Timepix4 for TEM, Dimova *et al.* [23] have previously measured the MTF at 100 kV and 200 kV acceleration voltages and improved the MTF using a clustering algorithm to reduce the effect from charge sharing. Ghosh *et al.* [24] have calculated the MTF and DQE at 300 kV using Monte-Carlo simulations of the electron trajectories in the sensor and discussed the influence of sensor thinning and different event threshold settings on the DQE and MTF.

In this work, the normalised noise power spectrum (NNPS) and DQE of a Timepix4 detector in TEM at 100 kV and 200 kV are measured. The NNPS is obtained from flat-field illumination datasets and subsequently the DQE is calculated from the measured NNPS and MTF using a slanted knife-edge as a deterministic input signal [23]. Initial experimental data using the Timepix4 detector to record data in a parallel-beam diffraction geometry from a sample of polycrystalline gold nanoparticles is also presented as an example application.

2 DQE Measurement

2.1 Detector System

The Timepix4 ASIC was bump-bonded to a 300 μm planar silicon sensor. The detector assembly was installed on a JEOL CryoARM Z300FSC TEM with the Merlin T4 readout system, the only commercially available readout system for the Timepix4, providing 81.92 Gbps FireFly optical readout. The per-pixel threshold for signal detection was set at 1000 electron-hole pairs in the sensor and a reverse-bias voltage of 100 V was applied.

In event-driven mode, the maximum detection speed is approximately 3.6 Mhits/ mm^2/s , which is limited by the transfer bandwidth [3]. The physical pixel size (pixel pitch) is 55 μm and number of pixels is 512×448 . The theoretical maximum number of events that can be detected (calculated by the maximum detection speed) is approximately 1.1×10^4 events/pixel/s. If the illumination is a uniform flat-field intensity across all pixels, the theoretical maximum current that can be measured on this detector is approximately 400 pA.

2.2 Methods

2.2.1 Flat-field Data Collection and Processing

Four flat-field datasets at 200 kV and five datasets at 100 kV were recorded and processed for calculation of the DQE. Each flat-field dataset was recorded with a 50 s exposure and the datasets were saved in .h5 file format as event lists. An event is a record of the energy deposition caused by an incident electron within a single pixel. Each event contains the pixel index and a timestamp [3] and an event list includes all events recorded within the exposure time on the detector.

The detector was evenly divided into two regions, top and bottom, each with 256×448 pixels. Sixteen .h5 files stored the event lists from the top region, and another sixteen files stored event lists from the bottom region.

The exposure time for a single acquisition was limited to approximately 60 s, which corresponds to the time required for a dataset to fill 512 GB of RAM on the control PC. To extend the total exposure time, multiple independent exposures with the same settings

were collected, stored, and preprocessed separately before being combined for the NPS calculation.

The datasets were then processed using the following steps:

1. Event lists stored in .h5 files for each dataset were merged and events in the processing area were converted into frames, each containing a target number of events (N_{tar}). Here ‘frames’ are defined as 2D image-like representations of the data formed by accumulating events in a pixel array.
2. Frames at the end of datasets containing fewer than the target number of events (N_{tar}) were discarded.
3. Frames at the same accelerating voltage from multiple datasets were combined and used to calculate the NPS spectrum and zero-frequency DQE.

The target number of events per frame (N_{tar}) was set to 5,000,000 (the summation of each frame generated from the event list is hence also 5,000,000). In theory, this value should be as low as possible, since a lower value makes the NPS calculation process closer to that handling single-electron events. A lower target number of events (N_{tar}) also results in a smoother NPS. However, if the value is too low, the number of frames increases, leading to higher computational time and storage requirements.

As also discussed later pixels along the 448-pixel side of the detector exhibit a higher response than the central area. We therefore selected a central area of 448×448 pixels on the detector for the NPS calculation as this gives a more faithful representation of the detector’s true performance in practical applications.

The frames converted from the event list can be represented as:

$$\begin{aligned}
 &c(f, x, y), \quad \text{where:} \\
 &f \in \{1, 2, \dots, N_f\}, \\
 &x \in \{1, 2, \dots, N_x\}, \\
 &y \in \{1, 2, \dots, N_y\},
 \end{aligned} \tag{1}$$

where f is the frame index, and x, y are the pixel indices. For the datasets considered in this work, as mentioned above, $N_x = N_y = 448$.

The characteristic properties of $c(f, x, y)$ are described by the parameters N_e and d_n . N_e represents the total number of events recorded in the detector area, and d_n represents the mean number of events per pixel per frame, as shown in Equation 2 and Equation 3:

$$N_e = \sum_{f=1}^{N_f} \sum_{x=1}^{N_x} \sum_{y=1}^{N_y} c(f, x, y), \tag{2}$$

$$d_n = \frac{1}{N_f N_x N_y} N_e. \tag{3}$$

2.2.2 Gain Factor Calculation

The average gain factor (g) is defined as the ratio of the total number of events recorded in the detector area (N_e) to the number of electrons that should have reached the effective area during an exposure time (N_c). This is not intrinsic to the detector signal gain, but a result of ‘charge-sharing’ when an electron is stopped in the bulk of the silicon sensor and

deposits charge in a number of pixels along its trajectory, creating a ‘cluster’ of events. Only the recorded number of events are counted and charge sharing was not compensated as described in reference [23]. The number of electrons was determined from the effective current (I_{ef}) and the exposure time (t), given in Equation 4. The average gain factor g was then calculated from Equation 5 as:

$$N_c = \frac{I_{ef} \cdot t}{e}, \quad (4)$$

$$g = \frac{N_e}{N_c}. \quad (5)$$

In Equation 4, e represents the charge of an electron. The effective current (I_{ef}) was obtained by multiplying the beam current by the ratio of the detector’s effective area to the total illuminating area of the beam. The exposure time (t) used in Equation 5 accounts only for those frames that contain the target number of events (N_{tar}).

2.2.3 NPS Calculation

To calculate the NPS, the first step is to compute a mean flat-field image $c_m(x, y)$ as:

$$c_m(x, y) = \frac{1}{N_f} \cdot \sum_{f=1}^{N_f} c(f, x, y). \quad (6)$$

The deviation of the frames from this mean flat-field image $c_m(x, y)$ is:

$$\Delta(f, x, y) = c(f, x, y) - c_m(x, y), \text{ broadcast over } f. \quad (7)$$

A 2D Fourier transform with respect to x and y is now performed to calculate the 2D NPS, as in Equation 8. Before performing the Fourier transform, a Hanning window function was applied to $\Delta(f, x, y)$ to reduce the effect of spectral leakage. Following the Fourier transform, the effect of the Hanning window on the amplitude is compensated.

$$\text{NPS}_{2D}(\omega_x, \omega_y) = \frac{1}{N_f} \cdot \sum_{f=1}^{N_f} |\mathcal{F}_{x,y}\{\Delta(f, x, y)\}|^2. \quad (8)$$

Since $N_x = N_y = 448$, the sampling of $\text{NPS}_{2D}(\omega_x, \omega_y)$ in ω_x and ω_y is the same, i.e. $\omega_x = \omega_y$.

The 1D NPS can then be computed as a radial average of the 2D NPS, representing a discretised approximation of:

$$\text{NPS}_{1D}(\omega_r) = \frac{1}{2\pi} \int_0^{2\pi} \text{NPS}_{2D}(\omega_r \cos \theta, \omega_r \sin \theta) d\theta, \quad (9)$$

where: $\omega_r = \sqrt{\omega_x^2 + \omega_y^2}$, $\theta = \arctan\left(\frac{\omega_y}{\omega_x}\right)$.

2.2.4 Estimation of NPS(0) and the NNPS

Since the mean value of a flat-field image was already subtracted from $\Delta(f, x, y)$ before computing the 2D NPS, the zero-frequency and near zero-frequency components (which correspond to slowly varying brightness in the image) have been removed. As a result,

the calculated NPS at zero frequency is underestimated. Therefore, the NPS value of the first and second frequency sampling points were also removed from the NPS curve.

NPS(0) can be computed separately by image binning [22, 25, 26]. The frame after binning $B_{Nb}(f, x, y)$ by a binning number N_b can be represented as:

$$B_{Nb}(f, x, y) = \sum_{a=1}^{N_b} \sum_{b=1}^{N_b} \Delta(f, N_b x + a, N_b y + b). \quad (10)$$

For the flat-field datasets used in this work, $B_{Nb}(f, x, y)$ was calculated from $N_b = 1$ to $N_b = 64$.

The variance of $B_{Nb}(f, x, y)$ is then calculated as σ_{Nb} :

$$\sigma_{Nb} = \text{Var}[B_{Nb}(f, x, y)] = \frac{1}{N_f N_x N_y} \sum_{f=1}^{N_f} \sum_{x=1}^{N_x} \sum_{y=1}^{N_y} (B_{Nb}(f, x, y) - \overline{B_{Nb}})^2, \quad (11)$$

where $\overline{B_{Nb}}$ is the mean value of all pixels in B_{Nb} .

As N_b increases, the value of $\frac{\sigma_{Nb}}{N_b^2}$ converges to a constant which is taken as the value of NPS(0). NPS_{2D} and NPS_{1D} are subsequently updated with this value at 0 spatial frequency.

The NNPS can be calculated by normalising the NPS using the calculated value of NPS(0) as:

$$\text{NNPS}(\omega) = \frac{\text{NPS}(\omega)}{\text{NPS}(0)}. \quad (12)$$

2.2.5 DQE Calculation

The DQE was calculated from both the MTF and NNPS. The MTF at 100 kV and 200 kV were measured following the method described in reference [23]. However, since the MTF and NNPS are both normalised at 0 spatial frequency, DQE(0) needs to be calculated separately and subsequently used to normalise the DQE values, as shown in Equation 13 and 14.

$$\text{DQE}(0) = \frac{d_n \cdot g}{\text{NPS}(0)} \quad (13)$$

In Equation 13, d_n is the mean event recorded per pixel defined in Equation 3 and g is the average gain factor defined in Equation 5. Then DQE(ω) was finally calculated as Equation 14 [18–20]:

$$\text{DQE}(\omega) = \text{DQE}(0) \times \frac{\text{MTF}^2(\omega)}{\text{NNPS}(\omega)}. \quad (14)$$

2.2.6 Ideal MTF and DQE

The ideal MTF, shown in Fig. 1, assumes that each pixel of the detector integrates all input events within the detection area without adding noise, meaning that the MTF is determined solely by the uniform sampling of the pixel shape. This ideal MTF ($\text{MTF}_{\text{ideal}}$) can be expressed as:

$$\text{MTF}_{\text{ideal}}(\omega) = \left| \frac{\sin(0.5\pi\omega)}{0.5\pi\omega} \right|. \quad (15)$$

For an ideal MTF without any consideration of noise, the output signal-to-noise ratio (SNR_{out}) depends only on the MTF applied to the input signal-to-noise ratio (SNR_{in}). In this case, the ideal DQE can be calculated as:

$$\text{DQE}_{\text{ideal}}(\omega) = \frac{\text{SNR}_{\text{in}}^2(\omega) \cdot \text{MTF}_{\text{ideal}}^2(\omega)}{\text{SNR}_{\text{in}}^2(\omega)} = \text{MTF}_{\text{ideal}}^2(\omega). \quad (16)$$

2.3 Results and Discussion

The measured DQE, MTF and NNPS as functions of frequency, from zero to the Nyquist frequency (ω_N), are plotted in Fig. 1 for which the DQE, NNPS, average gain factor g (defined by Equation 5) and the zero-frequency DQE were calculated from the flat-field datasets as described in Section 2.2.1. The MTF was measured as described in [23]. The relevant microscope settings and the average gain factor g for the flat-field datasets are listed in Table 1. The calculated values of DQE, MTF, NPS and NNPS at zero frequency, half the Nyquist frequency ($0.5\omega_N$) and the Nyquist frequency (ω_N) are listed in Table 2. These values are consistent with previously reported detector characterisations [22, 27–29] for the Medipix2 and Medipix3 sensors.

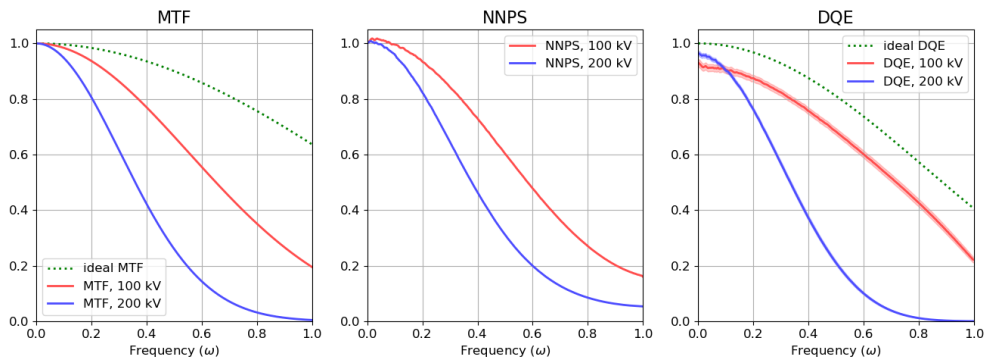


Figure 1: MTF, NNPS and DQE of Timepix4 detector for 100 kV and 200 kV electrons. X-axes are the fraction of spatial frequency to the Nyquist frequency of the detector. The ideal MTF and DQE curves are calculated as described in Section 2.2.6. The semi-transparent background of DQE curves indicates estimated uncertainties, as discussed in Section 2.4.1.

Table 1: Microscope settings and average gain factor (g) for flat-field datasets

Accelerating Voltage	100 kV	200 kV
Effective Beam current on detector, I_{ef}	14.4 pA	13.0 pA
Exposure time, t	248.7 sec	198.0 sec
Number of events on detector, N_e	56,155,000,000	77,595,000,000
Number of electrons by beam current, N_c ,	22,311,450,649	16,035,553,305
Average gain factor, g	2.517 ± 0.035	4.840 ± 0.038

Table 2: DQE, MTF, NNPS and NPS measured at zero frequency, half the Nyquist frequency ($0.5\omega_N$) and the Nyquist frequency (ω_N).

Frequency, ω	0	$0.5\omega_N$	ω_N
DQE, 200 kV	0.965 ± 0.008	0.210 ± 0.007	$(3.81 \pm 0.51) \times 10^{-4}$
DQE, 100 kV	0.931 ± 0.013	0.682 ± 0.012	0.221 ± 0.011
DQE, ideal	1.000	0.811	0.405
MTF, 200 kV	1*	0.260 ± 0.004	0.0046 ± 0.0003
MTF, 100 kV	1*	0.665 ± 0.004	0.195 ± 0.004
MTF, ideal	1*	0.900	0.637
NNPS, 200 kV	1*	0.3114 ± 0.0003	0.0533 ± 0.0001
NNPS, 100 kV	1*	0.6029 ± 0.0008	0.1602 ± 0.0002
NPS, 200 kV	124.9 ± 0.1	38.88 ± 0.02	6.654 ± 0.003
NPS, 100 kV	67.35 ± 0.07	40.61 ± 0.03	10.791 ± 0.006

*: Normalised value

The average gain factor g of the Timepix4 detector was measured as 2.517 at 100 kV and 4.840 at 200 kV using the threshold and reverse-bias settings in Section 2.1. This observed difference in the average gain factor g originates from charge sharing in which at higher electron energies, electrons deposit energy over a larger interaction volume and interact with more adjacent pixels in a cluster. Combined with a finite threshold, this leads to an increase in the number of recorded events and results in a larger measured average gain factor g . Further, this increased interaction volume also results in a broader point spread function for a single electron event and consequently reduces the MTF at 200 kV compared to 100 kV, as shown in Fig. 1.

For this reason, the experimental MTF can be enhanced and brought closer to the ideal MTF by applying a clustering algorithm [23, 30]. However, in this work, all measurements are based on the raw data from the Timepix4 detector without any clustering applied.

The NNPS, as shown in Fig. 1, is also affected by charge sharing which introduces spatial correlations between neighbouring pixels and effectively acts as a low-pass filter, suppressing high-frequency noise components. As a result, the NNPS measured at 200 kV shows a faster decline with increasing spatial frequency compared to that at 100 kV, for unchanged detector parameters.

With charge sharing affecting both the MTF and NNPS, the DQE at 100 kV has a value of 0.221 at the Nyquist frequency, where the ideal DQE (described in Section 2.2.6) is 0.405. However at 200 kV, the DQE at the Nyquist frequency is close to zero (3.81×10^{-4}) mainly because of the reduced MTF. At half the Nyquist frequency, as shown in Table 2, the DQE at 100 kV is 0.682, whereas at 200 kV it is 0.210, which is approximately one quarter of the ideal value of 0.811.

In the zero-frequency and low-frequency regions (below 1/10 of Nyquist frequency), the DQE at 200 kV is slightly higher than that at 100 kV. At zero frequency, the measured DQE(0) at 200 kV is 0.965, while at 100 kV it is only 0.931, as shown in Table 2. This is due to the 200 kV electrons having a greater chance than 100 kV to penetrate the aluminium contact layer on the detector surface. As a result, 100 kV electrons have a slightly lower probability of being recorded than 200 kV electrons. Therefore, the zero-frequency DQE, which represents the fraction of incident electrons detected by detector, is slightly lower at 100 kV than at 200 kV.

As previously noted, clustering algorithms designed to compensate for charge sharing

effects have been shown to improve the MTF of Timepix4 detectors [23, 30]. As the NNPS is also influenced by charge sharing, it is expected that such clustering algorithms may also improve the NPS and, consequently, the DQE.

The semitransparent background in Fig. 1 and the values indicated by ‘ \pm ’ in Table 1 and Table 2 represent the estimated uncertainties. The estimated uncertainties from zero to the Nyquist frequency in the DQE at 100 kV is less than 0.015 and at 200 kV is less than 0.010. A detailed description of uncertainty estimation is given in Section 2.4.

2.4 Uncertainty Estimation

2.4.1 Uncertainty in the DQE

The uncertainty in the DQE at each spatial frequency, $\sigma_{\text{DQE}}(\omega)$, was obtained using a standard first-order propagation of independent uncertainties in all contributing quantities. In Equation 17, σ_{DQE} is represented by uncertainties of the average gain factor g , the mean number of events per pixel per frame d_n , the NPS(ω), and the MTF(ω):

$$\sigma_{\text{DQE}}^2(\omega) = \left(\frac{\partial \text{DQE}}{\partial g}\right)^2 \sigma_g^2 + \left(\frac{\partial \text{DQE}}{\partial d_n}\right)^2 \sigma_{d_n}^2 + \left(\frac{\partial \text{DQE}}{\partial \text{MTF}}\right)^2 \sigma_{\text{MTF}}^2(\omega) + \left(\frac{\partial \text{DQE}}{\partial \text{NPS}}\right)^2 \sigma_{\text{NPS}}^2(\omega). \quad (17)$$

Based on Equation 17, Equation 13 and Equation 14, σ_{DQE} can be represented as:

$$\sigma_{\text{DQE}}(\omega) = k_{\text{DQE}}(\omega) \text{DQE}(\omega) \quad (18)$$

with k_{DQE} expressed as:

$$k_{\text{DQE}}(\omega) = \sqrt{\left(\frac{\sigma_g}{g}\right)^2 + \left(\frac{\sigma_{d_n}}{d_n}\right)^2 + \left(\frac{2\sigma_{\text{MTF}}(\omega)}{\text{MTF}(\omega)}\right)^2 + \left(\frac{\sigma_{\text{NPS}}(\omega)}{\text{NPS}(\omega)}\right)^2}. \quad (19)$$

The uncertainty in the MTF (σ_{MTF}) is determined through a Monte Carlo propagation of the edge-spread function (ESF) fit parameters; after fitting the ESF, random parameter vectors were sampled from the multivariate normal distribution defined by the best-fit parameters and their covariance. For each sample, the ESF, a line-spread function, and the resulting MTF were then recomputed. The spread of this ensemble at each spatial frequency provides the MTF standard deviation σ_{MTF} . To verify that the MTF uncertainty distribution is sufficiently symmetric for linear error propagation, the standard deviation was compared against the non-parametric 16th–84th percentile interval of the Monte-Carlo ensemble. The percentile-based half-width closely matches σ_{MTF} with a mean relative difference of $\ll 1$ across all spatial frequencies. Additionally, the RMS difference between the upper and lower percentile deviations normalised by the standard deviation is < 0.1 , indicating negligible skewness. Hence, the standard deviation was used as the MTF uncertainty term in the DQE error propagation and σ_{MTF} at 100 kV and 200 kV are plotted in Fig. 2.

The uncertainty in g was treated as a frequency independent scalar quantity. The value of g was calculated from the total number of events in all frames (N_e , defined in Equation 2) and the estimated number of electrons incident in the detector area during the exposure time (N_c , defined in Equation 4). The quantity N_e is a fixed value determined by the conversion of the event list into frames and by N_{tar} (see Section 2.2.1 Flat-field Data Collection and Processing). Consequently, the uncertainty in g is solely determined

by the uncertainty in the effective beam current measurement I_{ef} . The I_{ef} (13 to 14 pA as shown in Table 1) used here is close to the lower detection limit of the Faraday cup and the ammeter used and the uncertainty in I_{ef} is estimated to be 0.5 pA based on the precision of the ammeter. Finally, σ_g was calculated as $0.5/I_{ef}$, approximately 0.035 at 100 kV and 0.038 at 200 kV.

The uncertainty in the NPS was treated as per-frequency standard deviations derived from repeated measurements. The Bootstrap method was used to estimate the standard deviation of NPS. From all N_f flat-field frames, N_f frames were randomly resampled with replacement, and the frames selected in each sampling were treated as an independent dataset for the NPS calculation. This procedure was repeated n_{bs} times. Subsequently, the standard deviation at each spatial frequency was calculated from the n_{bs} independently computed NPS results. This standard deviation is then taken to be σ_{NPS} , plotted in Fig. 2 at 100 kV and 200 kV. The value of n_{bs} was set to 500 for the calculations in this work.

In Fig. 2, $\sigma_{\text{NPS}}(0)$ at both 100 kV and 200 kV are marked as dots on y-axis. This is because, in the Bootstrap method, $\sigma_{\text{NPS}}(0)$ were separately calculated by binning as described in Section 2.2.4, which results in a discontinuity at zero frequency.

The uncertainty of σ_{d_n} , number of events per pixel per frame, was calculated from the standard error of the mean (SEM) of all flat-field frames $c(f, x, y)$, as the SEM indicates by how much the d_n , the mean value of $c(f, x, y)$, is expected to vary from the true mean value under the current sample size. The σ_{d_n} was calculated as:

$$\sigma_{d_n} = \frac{s_c}{\sqrt{N_f N_x N_y}}, \quad (20)$$

where s_c is the standard deviation of $c(f, x, y)$ with s_c , d_n , σ_{d_n} and related parameters are listed in Table 3. This gives values of σ_{d_n} as 1.050×10^{-4} at 100 kV and 8.924×10^{-5} at 200 kV.

By substituting all the results for σ_g , σ_{d_n} , σ_{MTF} and σ_{NPS} into Equation 18 and Equation 19, k_{DQE} and σ_{DQE} can be then calculated and are plotted in Fig. 2.

Table 3: d_n , N_{tar} for DQE calculations

Accelerating Voltage	100 kV	200 kV
Target number of events per frame, N_{tar}	5,000,000	5,000,000
Number of frames, N_f	11,231	15,519
Average number of events per pixel per frame, d_n	24.91	24.91
Standard deviation of all pixels on all frames, s_c	4.985	4.980
SEM of all pixels on all frames, σ_{d_n}	1.050×10^{-4}	8.924×10^{-5}

The calculated σ_{DQE} at 100 kV and 200 kV are shown in Table 2 and in Fig. 1 as the semitransparent background of DQE curves. In general, the estimated uncertainty of measured DQE is less than 0.015 at 100 kV and 0.010 at 200 kV from zero frequency to the Nyquist frequency. The calculated σ_{MTF} , σ_{NPS} and σ_{NNPS} at half the Nyquist frequency ($0.5\omega_N$) and the Nyquist frequency (ω_N) are listed in Table 2.

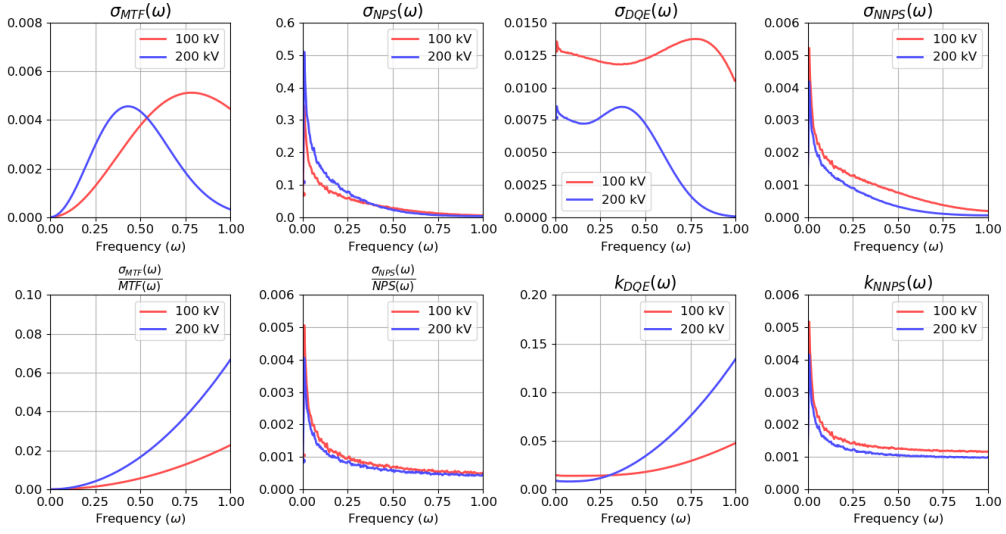


Figure 2: σ_{MTF} , σ_{NPS} , σ_{DQE} , σ_{NNPS} , $\frac{\sigma_{MTF}}{MTF}$, $\frac{\sigma_{NPS}}{NPS}$, k_{DQE} and k_{NNPS} for 100 kV and 200 kV. X-axes are the ratio of spatial frequency to the Nyquist sampling frequency of the detector. $\sigma_{NPS}(0)$ and $\frac{\sigma_{NPS}(0)}{NPS(0)}$ are marked as dots on y-axis.

2.4.2 Uncertainty in the NNPS

The uncertainty of NNPS for $\omega > 0$ is derived from Equation 12 using error propagation. Since NPS(0) is calculated independently of NPS(ω), their uncertainties, $\sigma_{NPS(0)}$ and $\sigma_{NPS(\omega)}$, are independent. Therefore, the error propagation can be expressed as in Equation 21.

$$\sigma_{NNPS}^2(\omega) = \left(\frac{\partial NNPS(\omega)}{\partial NPS(0)} \right)^2 \sigma_{NPS(0)}^2 + \left(\frac{\partial NNPS(\omega)}{\partial NPS(\omega)} \right)^2 \sigma_{NPS(\omega)}^2, \text{ when } \omega > 0 \quad (21)$$

The uncertainty $\sigma_{NNPS}(\omega)$ can be calculated by multiplying NNPS(ω) and $k_{NNPS}(\omega)$, as shown in Equation 22. Here, $k_{NNPS}(\omega)$ is expressed in terms of NPS(ω), NPS(0), $\sigma_{NPS}(\omega)$, and $\sigma_{NPS}(0)$, as given in Equation 23.

$$\sigma_{NNPS}(\omega) = k_{NNPS}(\omega) NNPS(\omega) \quad (22)$$

$$k_{NNPS}(\omega) = \sqrt{\frac{\sigma_{NPS}^2(0)}{NPS^2(0)} + \frac{\sigma_{NPS}^2(\omega)}{NPS^2(\omega)}} \quad (23)$$

The plots of $\sigma_{NNPS}(\omega)$ and $k_{NNPS}(\omega)$ are shown in Fig. 2. The values of σ_{NNPS} at $0.5\omega_N$ and ω_N are listed in Table 2. The σ_{NNPS} from zero to the Nyquist frequency is below 0.006, which is negligible compared to the calculated NNPS.

2.4.3 Other minor factors

In addition to the uncertainties considered above, the accuracy of the DQE measurement may also be affected by the following minor factors:

1. The total events in each dataset decreases with the duration of the data collection. During the approximately two-hour acquisition period used, multiple datasets showed a trend in which the total number of events in the final dataset acquired was approximately 0.5% lower than in the initial dataset. This was observed at both 100 kV and 200 kV and introduces an error in the calculation of the average gain factor (g). We believe that this effect is due to a reduction in the emission current of the cold-FEG over the duration of the acquisition.
2. As noted earlier the detector response is not uniform. The outer area, especially along the two 448-pixel edges, showed a slightly higher response compared to the central area which is primarily used in the measurements described. This results in an overestimation of the low-frequency component of the NPS. Therefore, only the central 448×448 pixels were used to reduce this skewing.
3. There are 45 dead pixels visible at 200 kV and 46 dead pixels at 100 kV where the value of a dead pixel is always 0. These dead pixels lead to a lower total number of events (N_e) and a slight underestimation of average gain factor (g). However, dead pixels account for only about 0.02% of all pixels within the 448×448 detector area, and thus the resulting underestimation of g due to dead pixels is also expected to be of the order of 0.02%. This error is much smaller than the uncertainty in g arising from the current measurement (I_{ef}) and was therefore neglected by the analysis described. In addition, since the NPS calculation is based on the deviation of the frames from the mean flat-field image (see Equation 7), dead pixels with zero values do not affect the NPS calculation.
4. The temperature of the detector chip increased from an initial value of 20 degree Celsius and stabilised at approximately 70 degree Celsius within two hours after the detector was initially powered on. The influence of temperature on the detector response was not measured, as no observable change in response was recorded during this period. Theoretically, the temperature affects only the mobility of charge carriers, rather than the number of electron-hole pairs generated. It has been reported that there is only a small temperature dependence in detector response parameters within typical operating ranges [31], suggesting that temperature effects are unlikely to be significant.

We believe that the amount of data collected in this work is sufficient to support the above statistical analysis. The number of events collected ranges from 5.6×10^{10} (100 kV) to 7.7×10^{10} (200 kV), as shown in Table 1, corresponding to an average of 2.8×10^5 (100 kV) and 3.8×10^5 (200 kV) events per pixel, respectively.

3 Parallel-Beam Diffraction

3.1 Experiment and results

As an initial demonstration of Timepix4 detector for electron diffraction, a polycrystalline diffraction pattern of a standard gold polycrystalline nanoparticle sample was recorded without a direct beam stop. A typical diffraction pattern is shown in Fig. 3(a) on a log-scale colormap.

The same microscope (JEOL CryoARM Z300FSC) and detector setting as for flat-field data were used to record diffraction data. Each diffraction pattern was recorded at 200 kV with a 20s exposure giving a total number of electrons at the sample of approximately 1.7×10^{10} and a fluence at the sample of approximately $3.2 \times 10^{-2} \text{ e}^-/\text{nm}^2$. However, since a selected area aperture and energy filter were used for data recording, the number of electrons on the detector was lower than on the sample. The number of events recorded was 184,227,225 with a corresponding number of electrons of 3.8×10^7 , estimated by the average gain factor g at 200 kV (4.840). Therefore, only about 0.2% of the electrons that are incident on the sample are recorded on the detector.

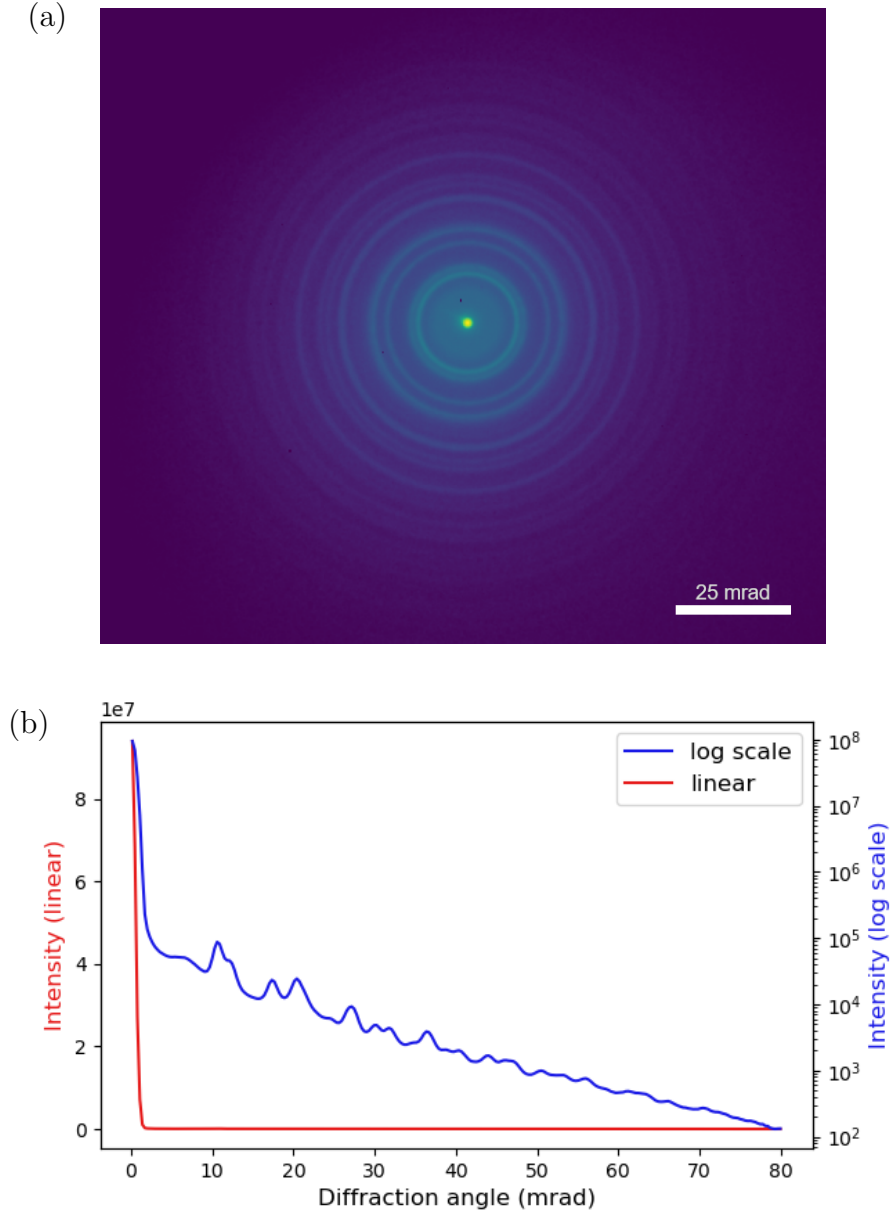


Figure 3: Parallel-Beam Diffraction pattern from a polycrystalline gold sample recorded on a Timepix4 detector at 200 kV and corresponding average radial line profiles. (a) Diffraction pattern recorded on a Timepix4 detector. Colormap is log-scale. (b) Average radial line profile of the diffraction pattern in (a), plotted on both linear (red line) and log scales (blue line).

Fig. 3(b) shows averaged radial line profiles from the diffraction pattern on a log-scale (blue) and a linear-scale (red) plotted on the same X-axis.

The 4 lowest angle reflections (corresponding to $\{111\}$, $\{200\}$, $\{220\}$, $\{311\}$) were used for calibration of the pixel size at the diffraction plane, giving a pixel size of 0.307 mrad/pixel. Reflections below 40 mrad are indexed and labelled in Fig. 4.

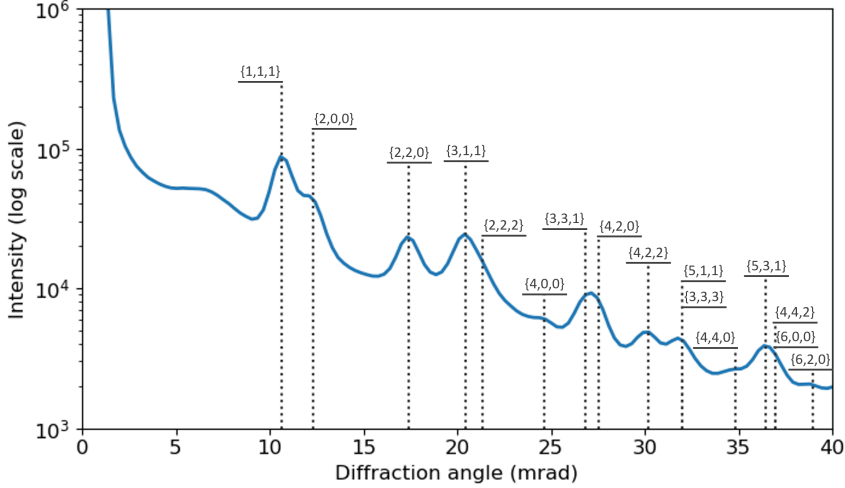


Figure 4: Average radial line profile of the diffraction pattern (0 to 40 mrad, corresponding to a limiting d-spacing of 0.06275 nm) and indexed gold reflections. The line profile is plotted on log scales. Indexed reflections are indicated by black dotted lines.

3.2 Discussion

Diffraction at angles higher than 40 mrad (corresponding to a d-spacing of approximately 0.06275 nm), average radial line profiles of the diffraction patterns for different angular ranges are shown in Fig. 5. The average radial line profile was processed using an Asymmetric Least Squares (ALS) method [32] (with parameters $\lambda = 100$, $p = 0.01$ and 100 iteration, mirror-padded at both ends) to remove the background. The intensity of the line profile was normalised to the intensity of the reflection $\{111\}$. In Fig. 5(a) the average line profile between angles 8 to 85 mrad (corresponding to d-spacings from approximately 0.3138 to 0.0295 nm) is plotted.

In Fig. 5(d), the average radial line profile of the diffraction pattern shows fluctuations in the relative intensity from 0 to approximately 1.2×10^{-3} . To determine whether this fluctuation is due to the overlapping of multiple diffraction peaks or simply noise, a simulated intensity distribution was calculated as shown as the green dashed curve in Fig. 5.

The simulated diffraction intensity distribution was calculated using the ReciPro software [33] using the FCC gold structure reported in [34] and electron scattering factors reported in [35]. An electron wavelength of 2.51 pm at 200 kV was used for calculations. Individual reflections were modelled using Gaussian functions. A standard deviation for the Gaussian function was set to 0.6 mrad for all reflections and the height of Gaussian functions used was proportional to the relative intensities of the reflections normalised by the $\{111\}$ intensity.

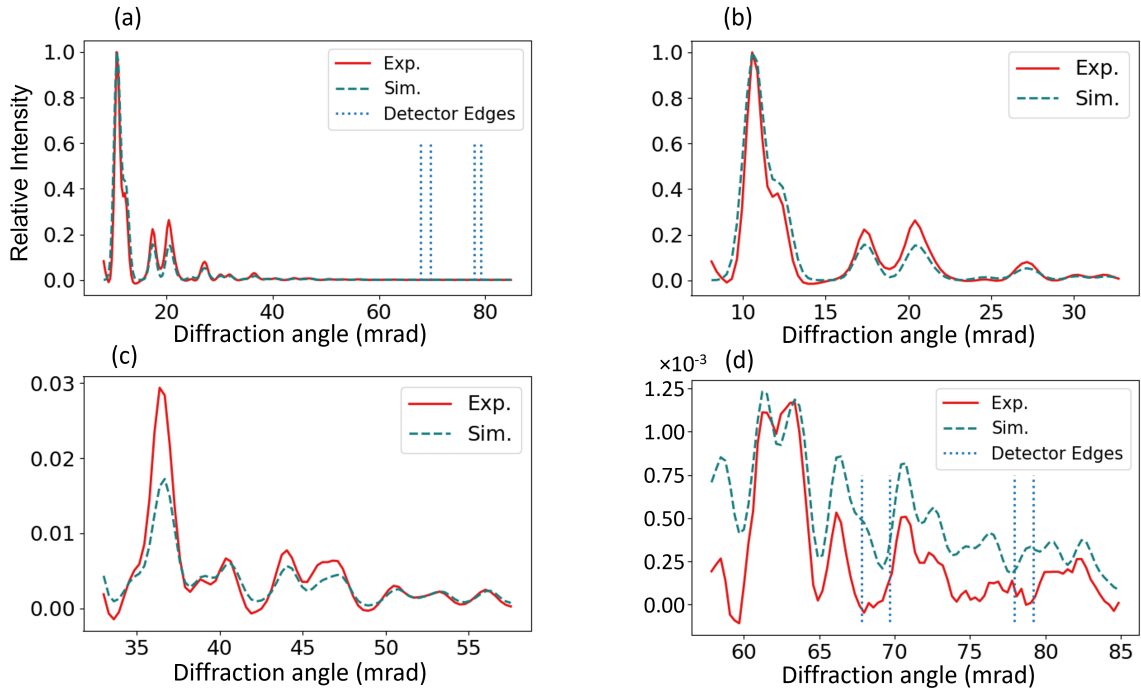


Figure 5: Experimental average radial line profile (red solid line, background removed) and simulated diffraction intensity distribution (green dash line). The blue dotted lines indicate the detector edges. (a) line profiles from 8 to 85 mrad (corresponding to d-spacings from 0.3138 to 0.0295 nm). (b), (c) and (d) line profiles in the range of 8 to 35 mrad (corresponding to d-spacings from 0.3138 to 0.0717 nm), 30 to 60 mrad (corresponding to d-spacing from 0.0837 to 0.0418 nm) and 55 to 85 mrad (corresponding to d-spacing from 0.0456 to 0.0295 nm), respectively with different y-axis scales applied.

The simulated diffraction distribution does not allow quantitative comparison, since many factors that affect the intensity distribution were not considered including, for example, crystal grain size and Debye-Waller factors. However, the simulated diffraction intensity distribution exhibits a trend similar to that of the experimentally obtained radial average line profile in the angle range of 60 to 75 mrad (corresponding to d-spacings from 0.0418 to 0.0335 nm), as shown in Fig. 5(d). This demonstrates that fluctuations in the diffraction data up to at least 75 mrad (corresponding to a d-spacing of 0.0355 nm) on the experimental line profile is not noise, but is formed from an overlap of diffracted intensities.

To quantitatively demonstrate the capability to resolve weak signals from diffraction patterns and average radial line profiles, the effective intensity span (C_e) of the line profile was calculated. The effective intensity span (C_e) was evaluated from the radial average line profile of the diffraction pattern, which defines maximum intensity (I_{max}) and the lowest resolvable intensity ($I_{min,r}$) in reciprocal space after angular integration. The value of C_e was then calculated using Equation 24. The intensity in this analysis indicates the total number of events recorded on a pixel, without clustering and other post-processing as:

$$C_e = \frac{I_{max}}{I_{min,r}}. \quad (24)$$

As discussed above, in Fig. 5(d), the radial average line profile shows diffraction information up to 75 mrad (corresponding to a d-spacing of 0.0355 nm). Therefore, the resolvable minimum intensity ($I_{min,r}$) for the average line profile is estimated as 186, the mean intensity at 75 mrad diffraction angle. The maximum intensity (I_{max}) is 1.143×10^7 at the centre beam. The effective intensity span (C_e) for the average line profile is then calculated as 6.15×10^4 .

However, the C_e using this calculation is underestimated. Approximately 27% of the events recorded at the centre beam pixel are recorded with a ‘pileup’ flag which means that this event has an abnormally high signal triggered in detector. This usually means multiple electrons arriving at a pixel within a short period of time such that the detector cannot separate them. As an estimation, the maximum intensity (I_{max}) could be at least 27% higher if every single electron is recorded separately. However, ‘pileup’ events do not influence the resolvable minimum intensity ($I_{min,r}$), since the number of ‘pileup’ events at a 75 mrad diffraction angle is 0.

This initial application shows the capability of the Timepix4 detector to resolve weak signals in electron diffraction patterns, achieving an effective intensity range of at least 6.15×10^4 . When combined with the detector’s high zero-frequency detective quantum efficiency (DQE) at greater than 0.9, the calculated effective intensity range shows that the detector has potential for detecting weak diffracted intensities.

It should be noted, however, that the effective intensity range reported in this demonstration is calculated from radial average line profile, rather than being calculated directly from individual pixels. This radial averaging reduces noise in pixels receiving a low number of electron events and hence the reported value should not be directly interpreted as the effective intensity range in the raw diffraction patterns.

4 Conclusion

In this work, the NNPS and DQE of a Timepix4 detector operated in a transmission electron microscope at 100 kV and 200 kV have been measured without clustering. The

zero-frequency DQE values were measured to be 0.931 at 100 kV and 0.965 at 200 kV. At the Nyquist frequency, the DQE at 100 kV is 0.22, whereas at 200 kV it decreases to 3.8×10^{-4} . Uncertainties of the DQE measurements are estimated to be less than 0.015 at 100 kV and less than 0.010 at 200 kV.

An example diffraction image recorded by the Timepix4 detector is also shown. The radial average line profile of the diffraction pattern shows diffracted information extending to at least 75 mrad (corresponding to a d-spacing of 0.0355 nm), with an effective intensity range in a calculated radial average of 6.15×10^4 . Given its fast readout speed, the Timepix4 detector is ideally suited for high-resolution, low-fluence electron diffraction.

5 Contributions

Zhiyuan Ding: Writing the manuscript; Review and editing; MTF, Flat-field and diffraction data recording; Flat-field and diffraction data analysis; Error estimation; Visualization.

Nina Dimova: Review and editing; MTF, Flat-field data recording; MTF data analysis; Error estimation.

Jonathan S. Barnard: Review and editing; MTF, Flat-field and diffraction data recording. Giulio Crevatin: Review and editing; MTF and Flat-field data recording; Software support.

Liam O’Ryan: Review and editing.

Richard Plackett: Review and editing.

Daniela Bortoletto: Review and editing.

Angus I. Kirkland: Review and editing; Overall project supervision.

Marcus Gallagher-Jones: Review and editing; MTF, Flat-field and diffraction data recording.

References

- [1] R. Ballabriga, M. Campbell, and X. Llopart, “An introduction to the Medipix family ASICs”, *Radiation Measurements* **136** (2020), 106271.
- [2] K. Heijhoff, K. Akiba, R. Ballabriga, et al., “Timing performance of the Timepix4 front-end”, *Journal of Instrumentation* **17**.(07) (2022), P07006.
- [3] X. Llopart, J. Alozy, R. Ballabriga, et al., “Timepix4, a large area pixel detector readout chip which can be tiled on 4 sides providing sub-200 ps timestamp binning”, *Journal of Instrumentation* **17**.(01) (2022), C01044.
- [4] K. Akiba, J. Alozy, D. Bacher, et al., “The Timepix4 beam telescope”, *Nuclear Instruments and Methods in Physics Research Section A: Accelerators, Spectrometers, Detectors and Associated Equipment* **1084** (2026), 171234.
- [5] P. Delogu, N. V. Biesuz, R. Bolzonella, et al., “Validation of Timepix4 energy calibration procedures with synchrotron X-ray beams”, *Nuclear Instruments and Methods in Physics Research Section A: Accelerators, Spectrometers, Detectors and Associated Equipment* **1068** (2024), 169716.
- [6] Y. Chushkin, J. Correa, A. Ignatenko, et al., “Achieving nanosecond time resolution with a two-dimensional X-ray detector”, *Synchrotron Radiation* **32**.(5) (2025).

- [7] J. Correa, A. Ignatenko, D. Pennicard, et al., “TEMPUS, a Timepix4-based system for the event-based detection of X-rays”, *Synchrotron Radiation* **31**.(5) (2024).
- [8] R. Bolzonella, J. Alozy, R. Ballabriga, et al., “Development and characterization of hybrid MCP-PMT with embedded Timepix4 ASIC used as pixelated anode”, *Nuclear Instruments and Methods in Physics Research Section A: Accelerators, Spectrometers, Detectors and Associated Equipment* (2025), 170965.
- [9] R. Bolzonella, J. Alozy, R. Ballabriga, et al., “Timing resolution performance of Timepix4 bump-bonded assemblies”, *Journal of Instrumentation* **19**.(07) (2024), P07021.
- [10] L. A. Cerbone, L. Cimmino, A. Sarno, et al., “Monte Carlo and experimental evaluation of a Timepix4 compact gamma camera for coded aperture nuclear medicine imaging with depth resolution”, *Physica Medica* **113** (2023), 102663.
- [11] D. Jannis, C. Hofer, C. Gao, et al., “Event driven 4D STEM acquisition with a Timepix3 detector: Microsecond dwell time and faster scans for high precision and low dose applications”, *Ultramicroscopy* **233** (2022), 113423.
- [12] G. Li, M. Xu, W. Tang, et al., “Atomically resolved imaging of radiation-sensitive metal-organic frameworks via electron ptychography”, *Nature Communications* **16**.(1) (2025), 914.
- [13] A. Annys, H. L. L. Robert, S. Gholam, et al., “Removing constraints of 4D-STEM with a framework for event-driven acquisition and processing”, *Ultramicroscopy* (2025), 114206.
- [14] V. Migunov, H. Ryll, X. Zhuge, et al., “Rapid low dose electron tomography using a direct electron detection camera”, *Scientific reports* **5**.(1) (2015), 14516.
- [15] S. Koneti, L. Roiban, F. Dalmas, et al., “Fast electron tomography: Applications to beam sensitive samples and in situ TEM or operando environmental TEM studies”, *Materials Characterization* **151** (2019), 480–495.
- [16] M. Gallagher-Jones, K. Bastillo, C. Ophus, et al., “Atomic structures determined from digitally defined nanocrystalline regions”, *IUCrJ* **7**.(3) (2020), 490–499.
- [17] N. Vlahakis, S. Qu, L. S. Richards, et al., “Fast event-based electron counting for small-molecule structure determination by MicroED”, *Crystal Structure Communications* **81**.(3) (2025).
- [18] R. R. Meyer and A. I. Kirkland, “The effects of electron and photon scattering on signal and noise transfer properties of scintillators in CCD cameras used for electron detection”, *Ultramicroscopy* **75**.(1) (1998), 23–33.
- [19] R. R. Meyer, A. I. Kirkland, R. E. Dunin-Borkowski, et al., “Experimental characterisation of CCD cameras for HREM at 300 kV”, *Ultramicroscopy* **85**.(1) (2000), 9–13.
- [20] R. R. Meyer and A. I. Kirkland, “Characterisation of the signal and noise transfer of CCD cameras for electron detection”, *Microscopy Research and Technique* **49**.(3) (2000), 269–280.
- [21] A. I. Ruskin, Z. Yu, and N. Grigorieff, “Quantitative characterization of electron detectors for transmission electron microscopy”, *Journal of structural biology* **184**.(3) (2013), 385–393.

- [22] G. McMullan, S. Chen, R. Henderson, et al., “Detective quantum efficiency of electron area detectors in electron microscopy”, *Ultramicroscopy* **109**.(9) (2009), 1126–1143.
- [23] N. Dimova, R. Plackett, D. Weatherill, et al., “Measurement of the resolution of the Timepix4 detector for 100keV and 200keV electrons for transmission electron microscopy”, *Nuclear Instruments and Methods in Physics Research Section A: Accelerators, Spectrometers, Detectors and Associated Equipment* **1075** (2025), 170335.
- [24] R. Ghosh, S. E. Zeltmann, and D. A. Muller, “Optimizing an Event-Driven Detector for High Speed Scanning Diffraction Measurements in the Transmission Electron Microscope” ().
- [25] O. Marcelot, C. Marcelot, and S. Rolando, “Limitations and drawbacks of DQE estimation methods applied to electron detectors”, *Microscopy* **73**.(5) (2024), 405–413.
- [26] K. A. Paton, “Studies of hybrid pixel detectors for use in Transmission Electron Microscopy”, PhD thesis, University of Glasgow, 2023.
- [27] G. McMullan, D. M. Cattermole, S. Chen, et al., “Electron imaging with Medipix2 hybrid pixel detector”, *Ultramicroscopy* **107**.(4-5) (2007), 401–413.
- [28] J. A. Mir, R. Clough, R. MacInnes, et al., “Characterisation of the Medipix3 detector for 60 and 80 keV electrons”, *Ultramicroscopy* **182** (2017), 44–53.
- [29] K. A. Paton, M. C. Veale, X. Mu, et al., “Quantifying the performance of a hybrid pixel detector with GaAs: Cr sensor for transmission electron microscopy”, *Ultramicroscopy* **227** (2021), 113298.
- [30] J. P. van Schayck, E. van Genderen, E. Maddox, et al., “Sub-pixel electron detection using a convolutional neural network”, *Ultramicroscopy* **218** (2020), 113091.
- [31] W. Rose, *A Temperature Dependent Study of the Calibration of Timepix4 Assemblies*, Oct. 2024.
- [32] P. H. C. Eilers and H. F. M. Boelens, “Baseline correction with asymmetric least squares smoothing”, *Leiden University Medical Centre Report* **1**.(1) (2005), 5.
- [33] Y. Seto and M. Ohtsuka, “ReciPro: free and open-source multipurpose crystallographic software integrating a crystal model database and viewer, diffraction and microscopy simulators, and diffraction data analysis tools”, *Applied Crystallography* **55**.(2) (2022), 397–410.
- [34] I. Suh, H. Ohta, and Y. Waseda, “High-temperature thermal expansion of six metallic elements measured by dilatation method and X-ray diffraction”, *Journal of Materials Science* **23**.(2) (1988), 757–760.
- [35] L.-M. Peng, G. Ren, S. L. Dudarev, et al., “Robust parameterization of elastic and absorptive electron atomic scattering factors”, *Foundations of Crystallography* **52**.(2) (1996), 257–276.